Supporting Information

Synergistic coupling of interface ohmic contact and LSPR effects regulates over Au/Bi$_{24}$O$_{31}$Br$_{10}$ nanosheets for visible-light-driven photocatalytic CO$_2$ reduction to CO

Jie Liu, Yu Xie*, Yiqiao Wang, Kai Yang, Shuping Su, Yun Ling, Pinghua Chen

School of Environmental and Chemical Engineering, Nanchang Hangkong University

No. 696 South Fenghe Avenue, Nanchang, Jiangxi Province, China, 330063
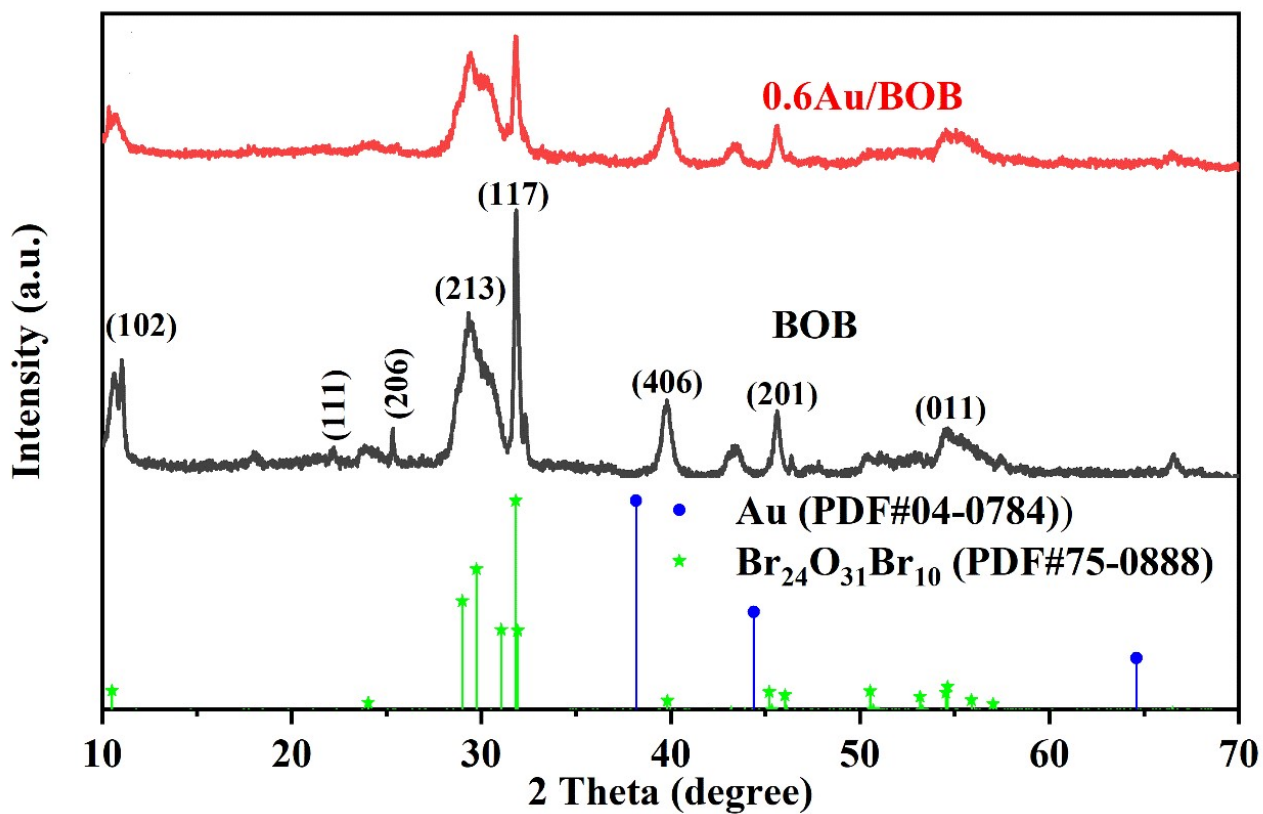
* Contact: xieyu_121@163.com

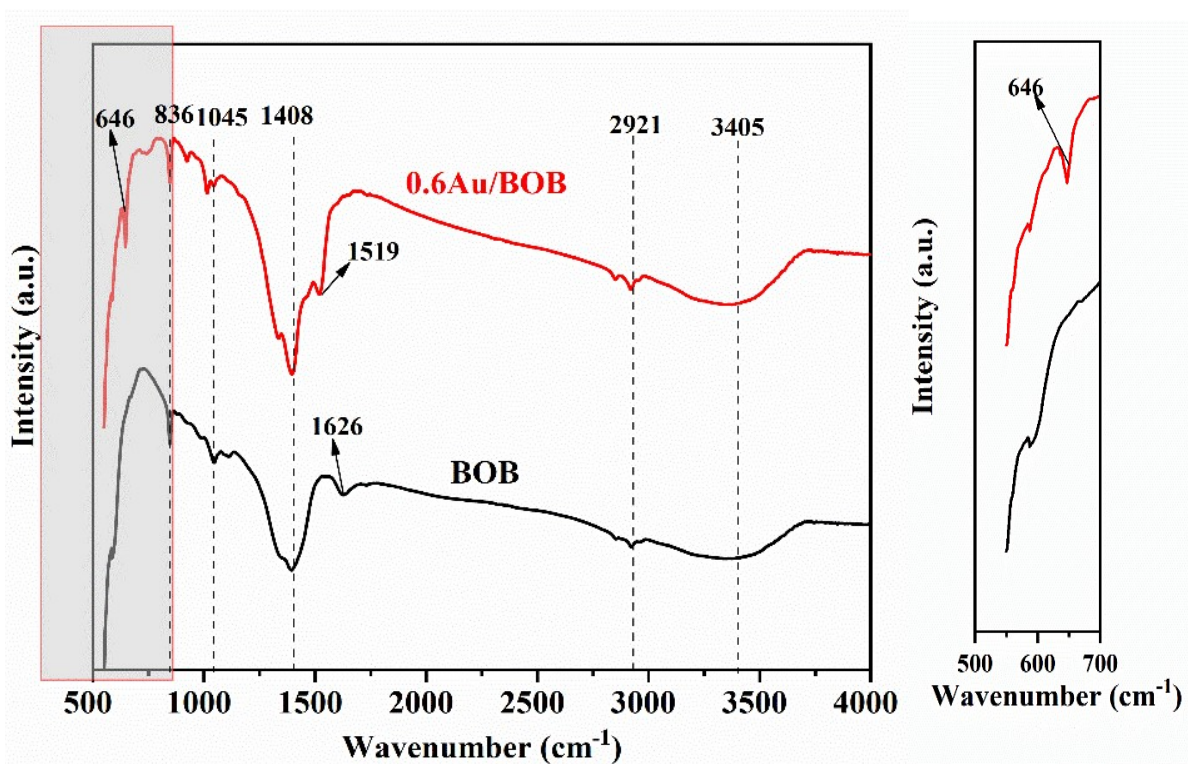**Fig. S1.** XRD patterns of BOB and 0.6Au/BOB photocatalysts.

Fig. S2. FTIR patterns of BOB and 0.6Au/BOB photocatalysts.

The chemical structure information of BOB and 0.6Au/BOB was also analyzed by FTIR. **Fig. S2** shows that the peaks of 836 and 1408 cm^{-1} belong to the vibrational state of Bi-O bond and Bi-Br bondC. The peaks at 1045 and 2921 cm^{-1} belong to the stretching state of C=O and the vibration state of C=H [1]. In addition, the characteristic peaks at 1519, 1626 and 3405 cm^{-1} originate from water molecules and hydroxyl groups. Thus, the 0.6Au/BOB composite shows a new characteristic peak at 661 cm^{-1}, corresponding to the Au-Bi-O vibrational state, which further confirms the successful synthesis of the composite photocatalyst.
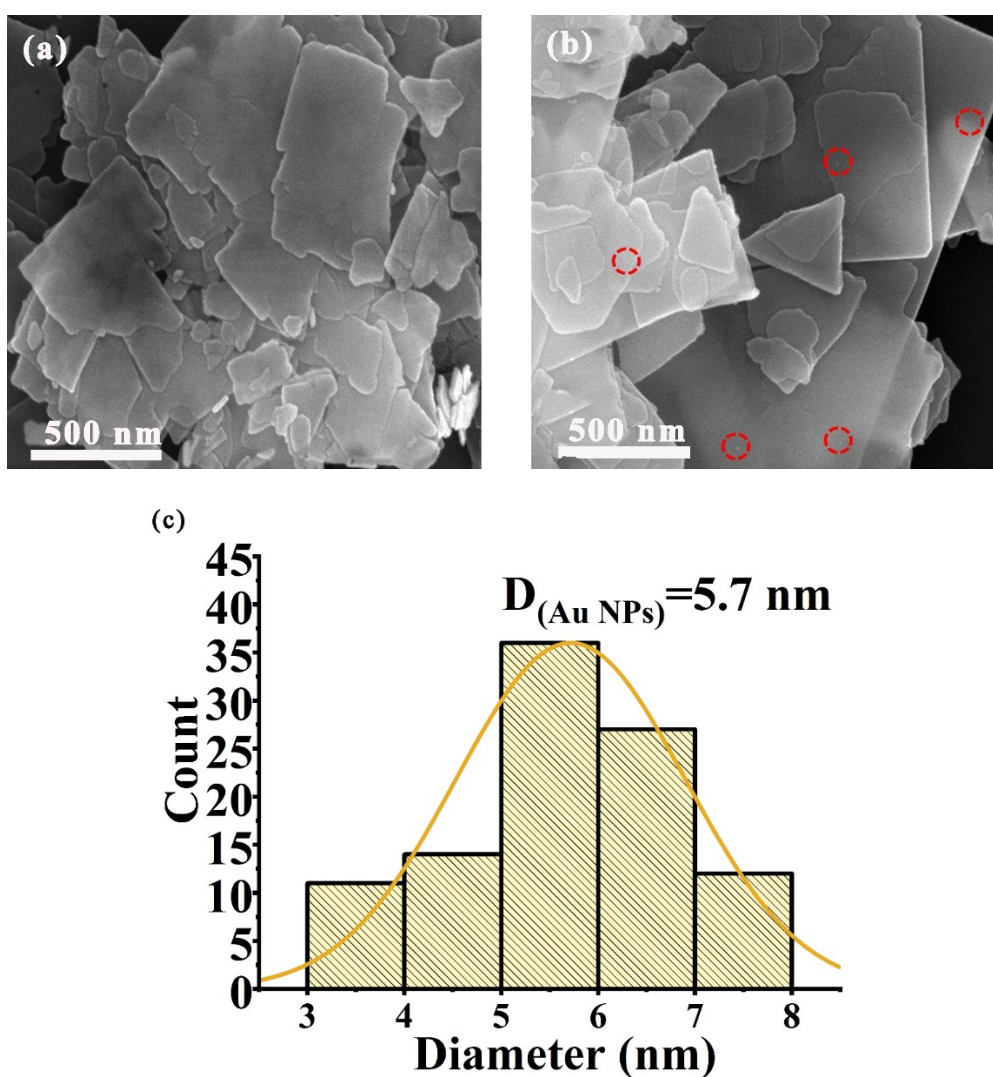

Fig. S3. SEM images of (a) BOB and (b) 0.6Au/BOB; (c) Size distribution of Au NPs.
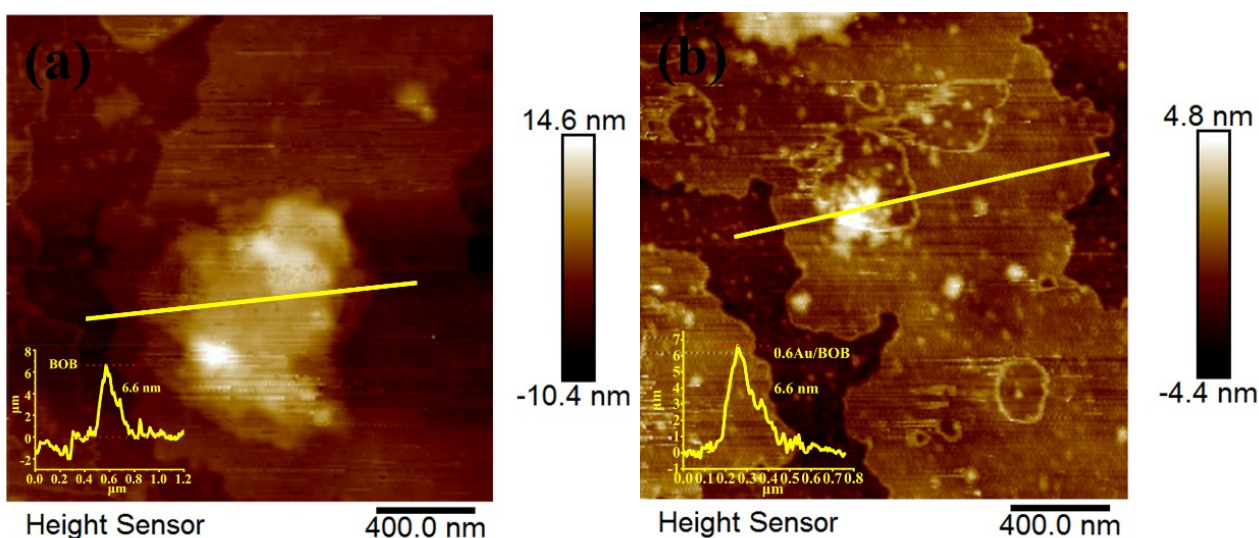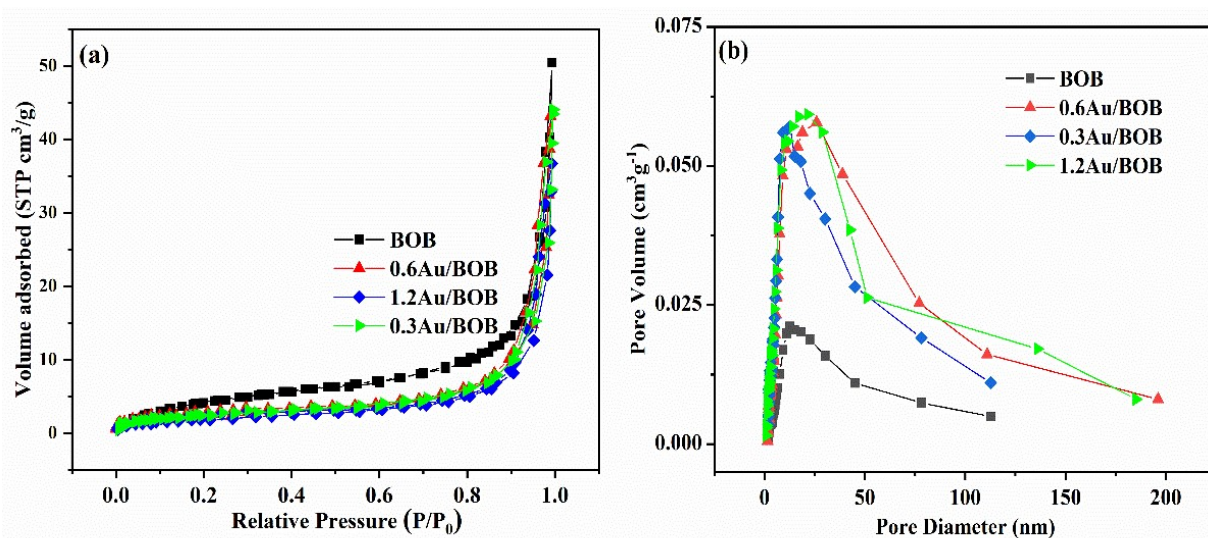
Fig. S4. AFM images of BOB and 0.6Au/BOB.

Fig. S5. (a) N_2 adsorption-desorption isotherms and (b) pore diameter distribution of BOB, 0.3Au/BOB, 0.6Au/BOB and 1.2Au/BOB.

By using N_2 adsorption-desorption experiments, the specific surface area and pore size distributions of the samples were measured. As shown in **Fig. S5a-b**, BOB, 0.3Au/BOB, 0.6Au/BOB and 1.2Au/BOB exhibit type IV adsorption isotherms and H3 hysteresis loops [2], indicating mesopore structure. The specific surface areas of BOB, 0.3Au/BOB, 0.6Au/BOB and 1.2Au/BOB are displayed in **Table S2** at 3.995, 5.636, 7.874 and 9.634 m^2g^{-1}, respectively. Among them, Au/BOB composite has a larger specific surface area than the pure BOB, which can be attributed to the fine distribution of Au NPs on its surface. The fine dispersion of Au NPs on the surface makes the Au/BOB composite

has a larger surface area than pure BOB. Meanwhile, further comparison between **Fig.4a** and **Table S2** shows that although the performance of 0.6Au/BOB is the highest, the specific surface area is not the highest, which shows that the specific surface area does not significantly affect the performance of Au/BOB composite.
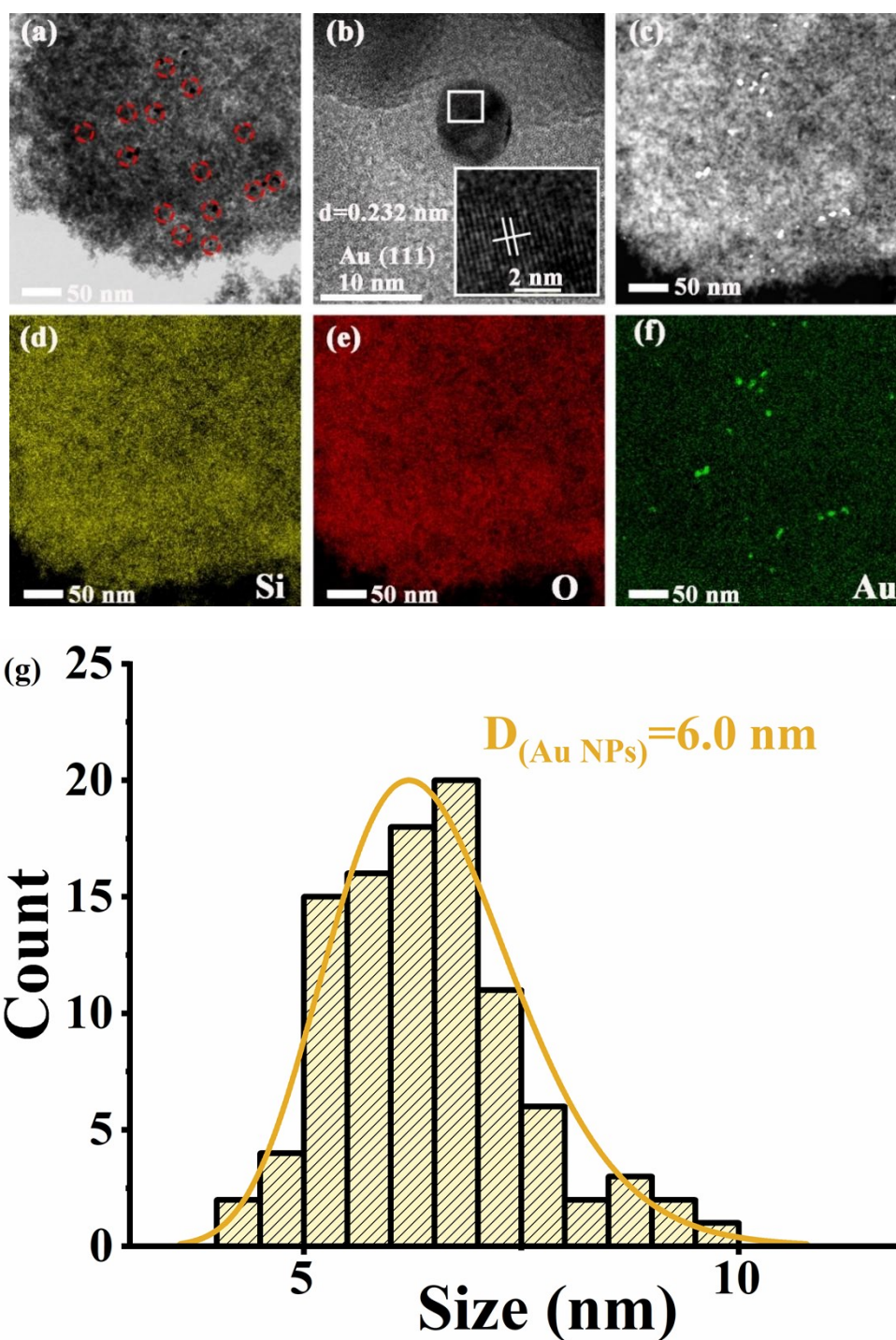

Fig. S6. TEM images of (a-f) 0.6Au/SiO$_2$; (g) Size distribution of Au NPs.
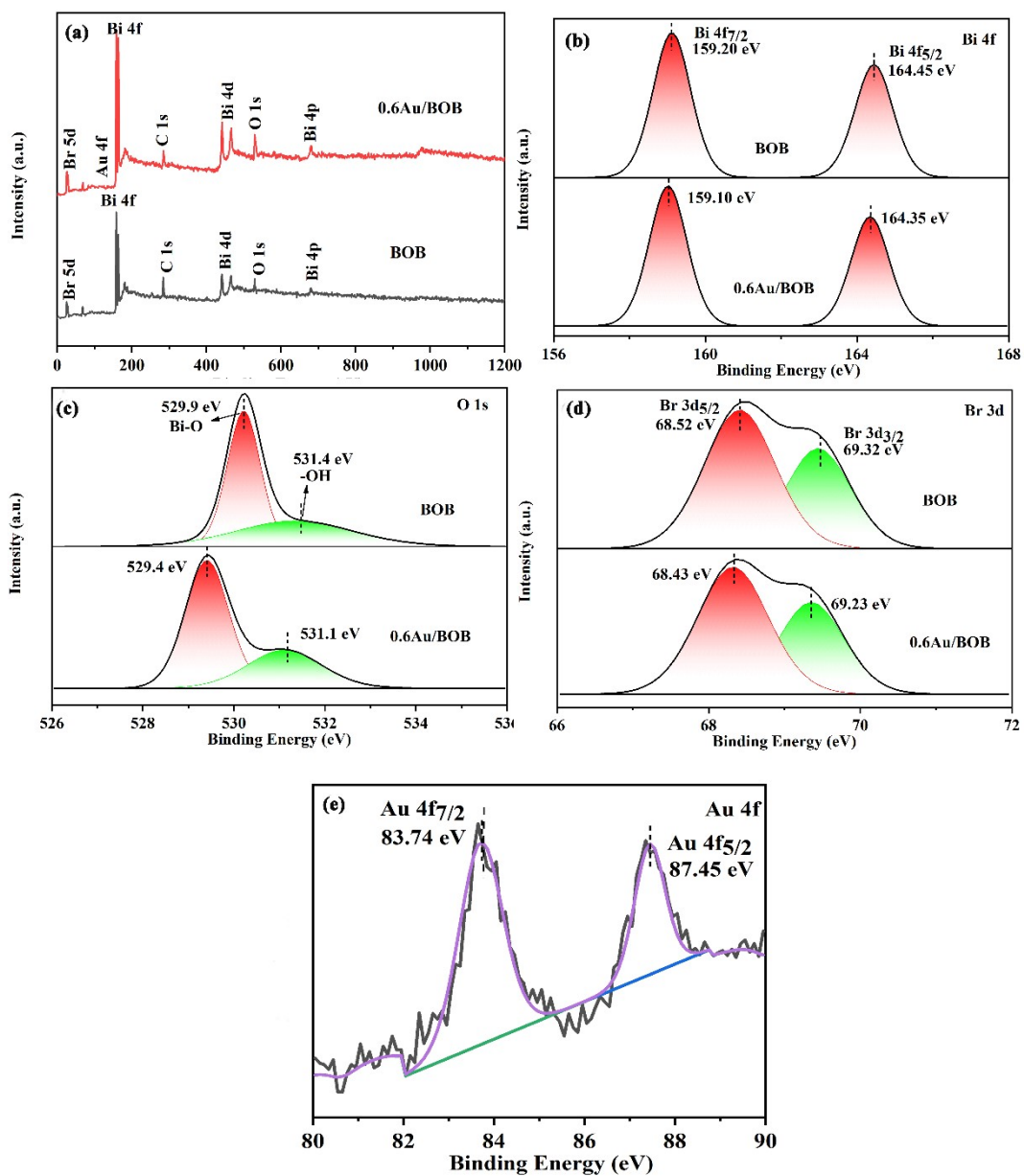
Fig. S7. High-resolution XPS spectra of (a) survey, (b) Bi 4f, (c) O 1s, (d) Br 3d and (e) Au 4f for BOB and 0.6Au/BOB.
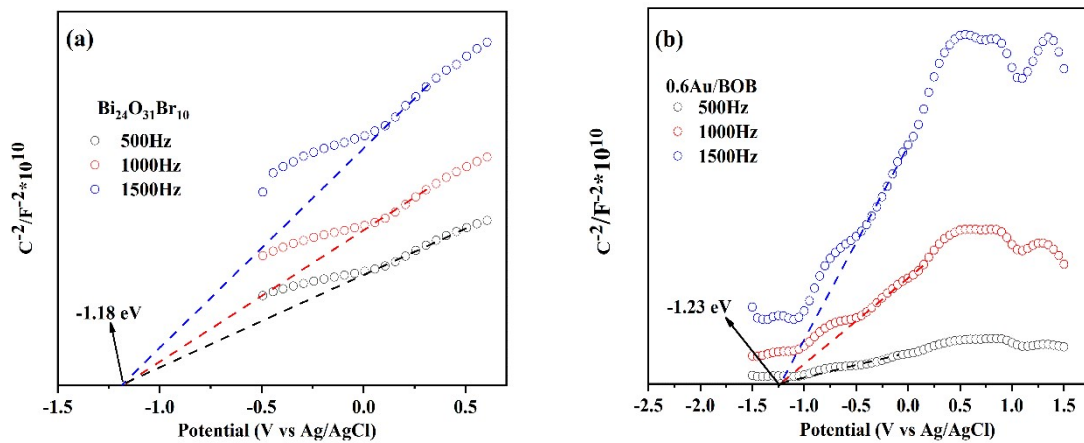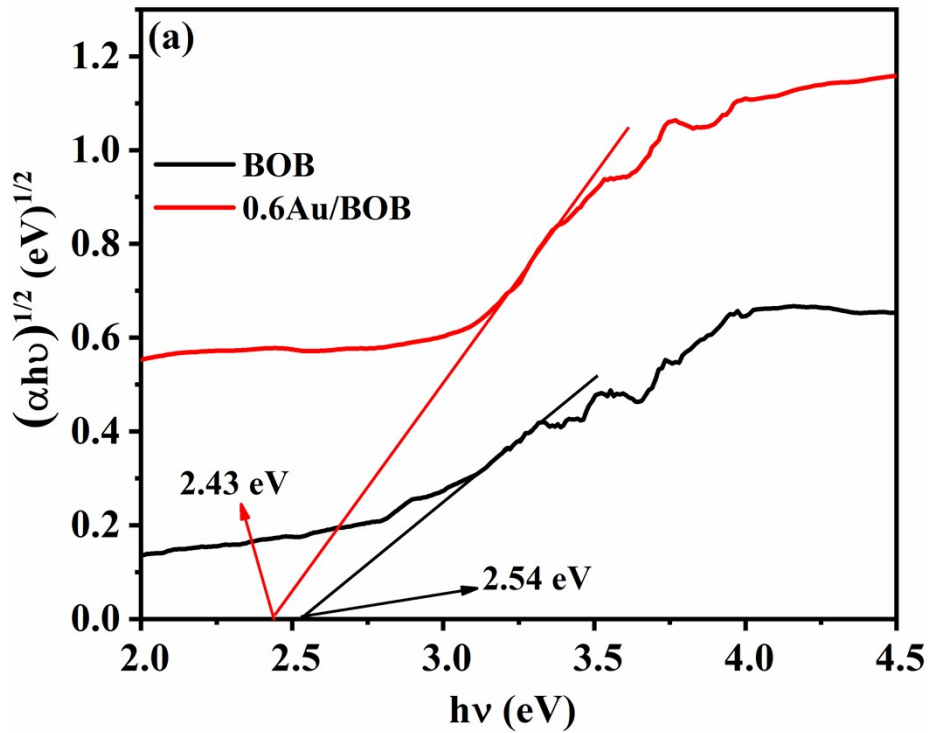
Fig. S8. (a) The band gap of BOB and 0.6Au/BOB; Mott-Schottky plots of (a) BOB and (b) 0.6Au/BOB at various frequencies.

The band gap values of BOB and 0.6Au/BOB can be obtained according to UV-vis DRS spectrum and the following Tauc curve [2]:

$$(\alpha h\nu)^{1/n} = A (h\nu - E_g) \tag{1}$$

where α, $h\nu$, A and E_g represent absorption coefficient, photon energy, constant and band gap, respectively. Since BOB is indirect semiconductors, the value of n is 2. Therefore, the band gap of

BOB and 0.6Au/BOB were calculated to be 2.54 and 2.43 eV (**Fig. S8a**), respectively, which were consistent with those reported in the literature. To further determine the possible band gap structure of the samples, the flat band potential (E_{FB}) of BOB and 0.6Au/BOB was analyzed using the Mott-Schottky curve. As shown in **Fig. S8b-c**, the positive slope of Mott-Schottky curve indicated that BOB is all n-type semiconductors. The CB potential (E_{CB}) of n-type semiconductors was like that of E_{FB}. According to the equation of $E_{VB} = E_g + E_{CB}$, the E_{CB} of BOB and 0.6Au/BOB were -1.18 and-1.23 eV vs. Ag/AgCl (-0.97 and-1.02 V vs. NHE), respectively. The valence band potentials (E_{VB}) of BOB and 0.6Au/BOB were estimated are 1.36 and 1.20 eV vs. Ag/AgCl (1.57 and 1.41 V vs. NHE), respectively. With the loading of Au NPs, the E_{CB} of 0.6Au/BOB shifts upward, indicating the enhanced reduction of CO_2-CO (CO_2/CO=-0.53 V).
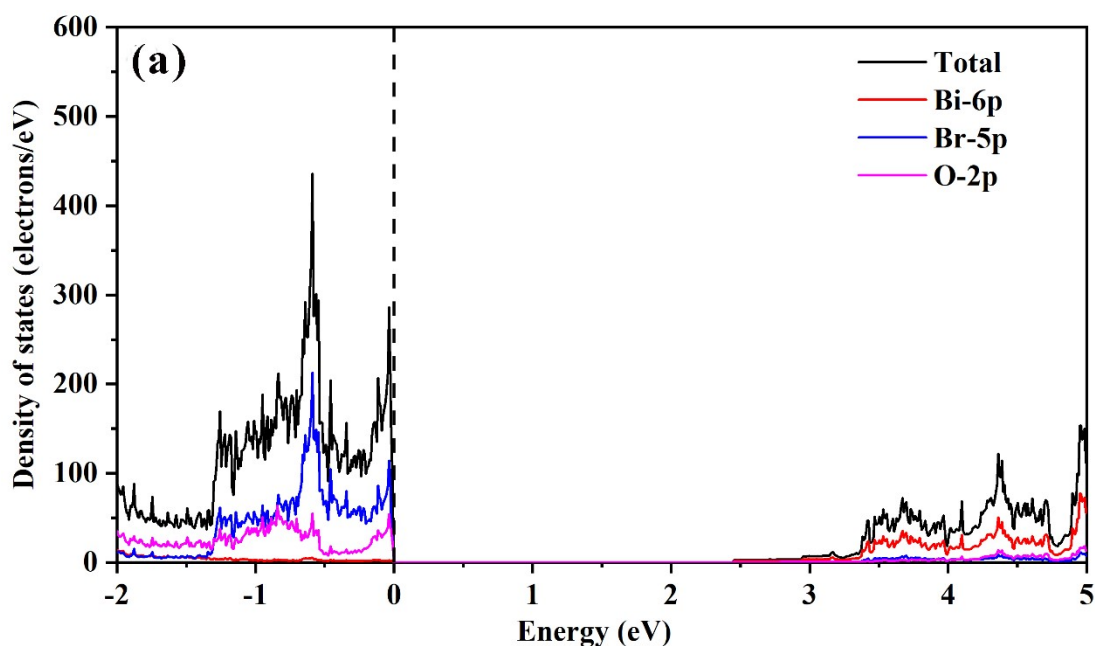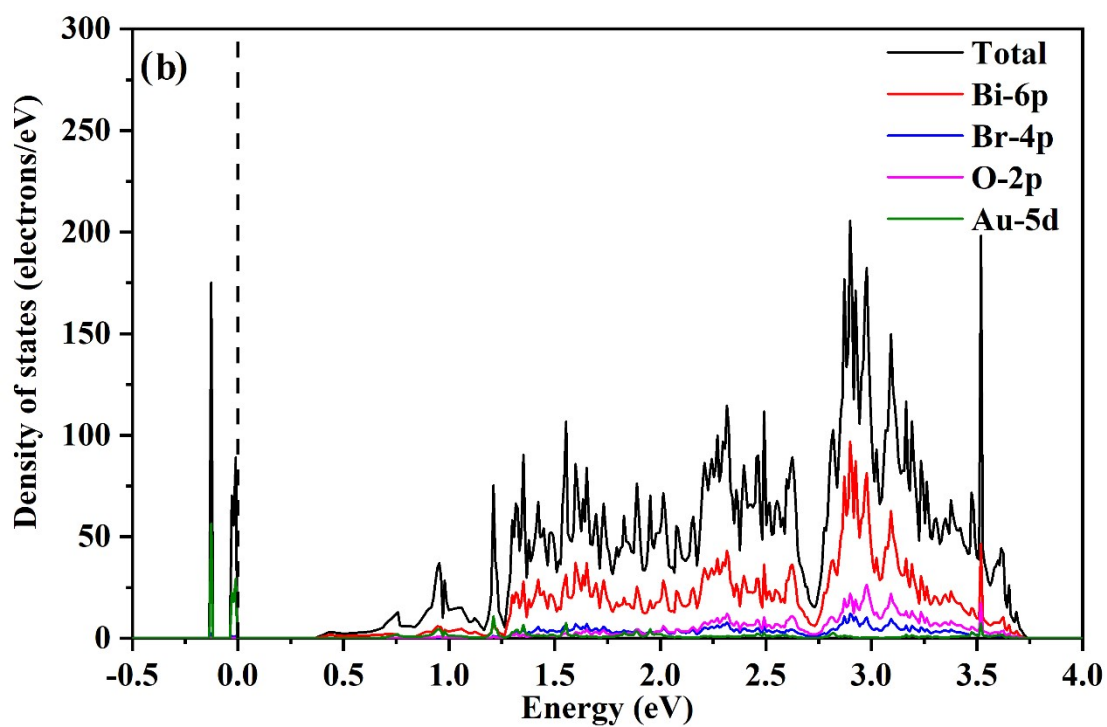
Fig. S9. Calculated DOS of (a) BOB and (b) Au/BOB composite.
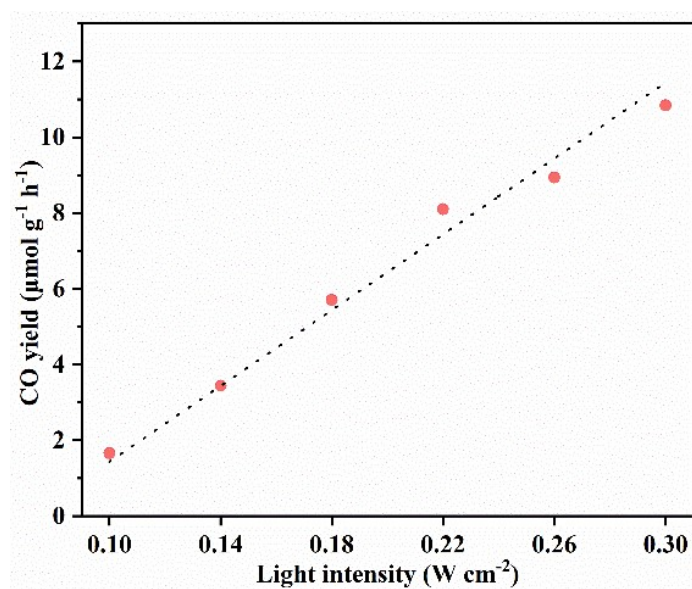
Fig. S10. CO yield plotted as a function of light intensity.
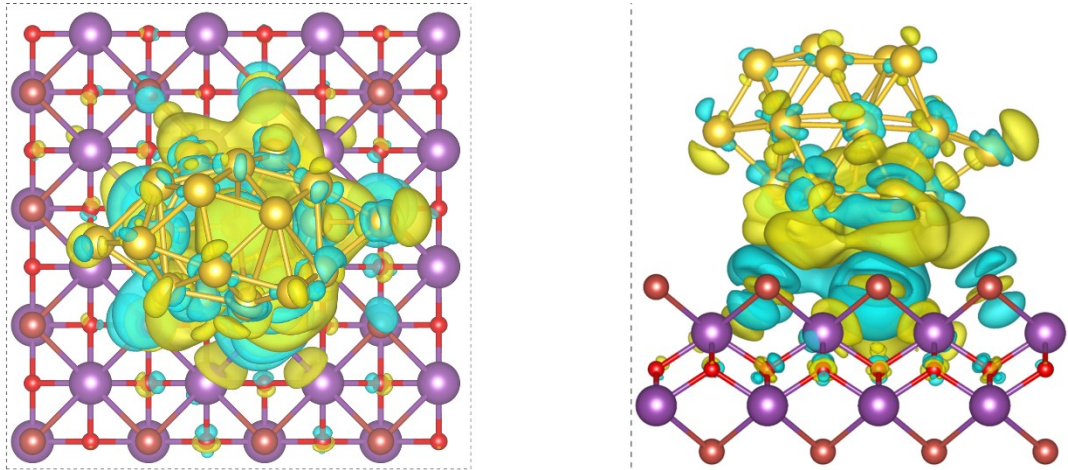
Fig. S11. Top and side view of charge density difference of BOB loading AuNPs. Charge accumulation and depletion are marked by cyan and yellow area, respectively. The isosurface level is 5E-4 eÅ^{-3}.
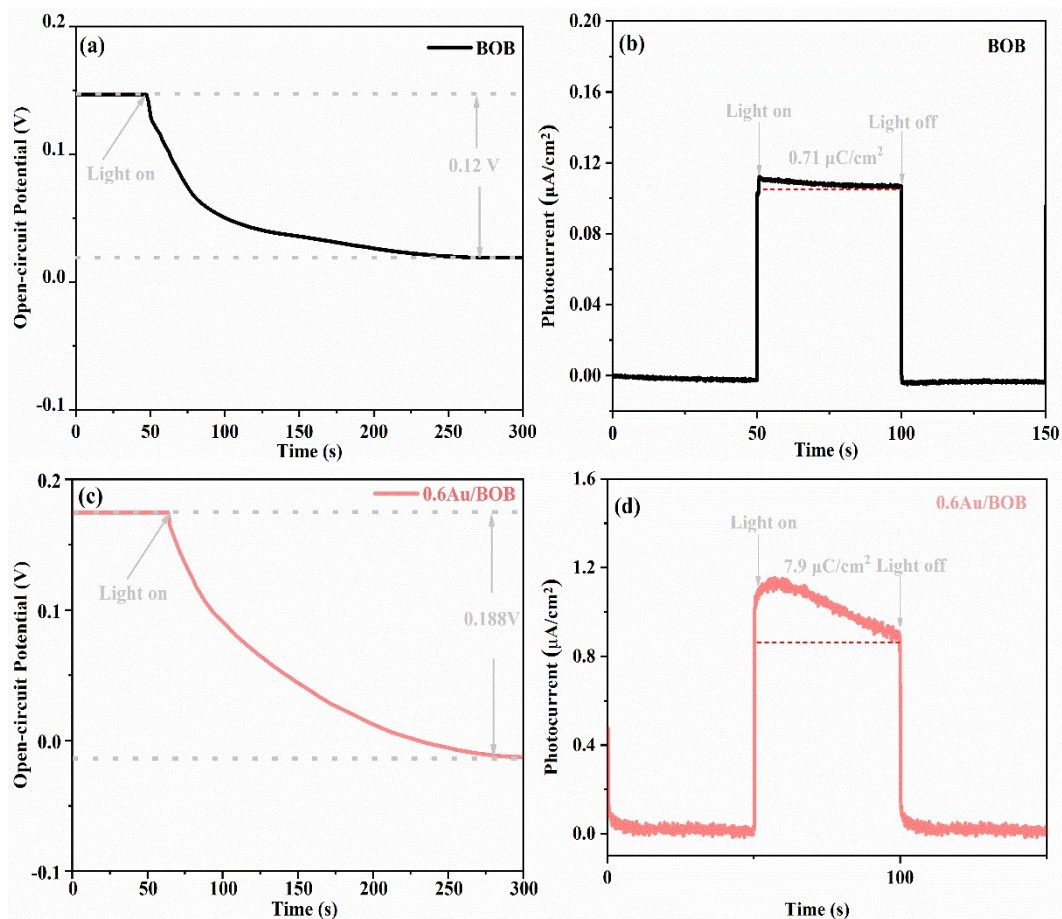
Fig. S12. (a) The surface voltage of BOB; (b) the surface accumulated electrons density of BOB; (c) the surface voltage of 0.6Au/BOB; (d) the surface accumulated electrons density of 0.6Au/BOB.

The internal electrical field intensity is calculated based on equation [3]:

$$F_s=(-2V_s\rho/\varepsilon\varepsilon_0)^{1/2} \qquad\qquad (2)$$

where F_s is the internal electrical field magnitude, V_s is the surface voltage, ρ is the surface charge density, ε is the low frequency dielectric constant, and ε_0 is the permittivity of free space. Because the ε and ε_0 are constants, the internal electrical field magnitude can be determined by the surface voltage and the surface charge density. The surface charge density can be obtained by the integral of the transient anodic photocurrent peak. The surface voltage can be measured by the open-circuit potentials. So, we can qualitatively compare the internal electrical field magnitude according to the $(V_s\rho)^{1/2}$ values.
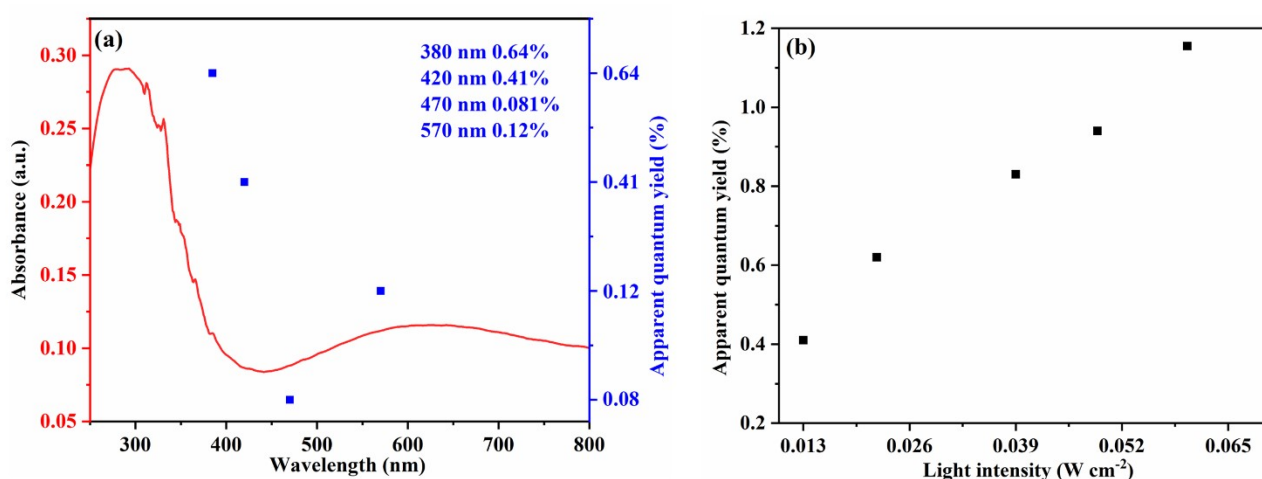
Fig. S13. (a) Wavelength and (b) light intensity-dependent apparent quantum yield (AQY) of 0.6Au/BOB.

Fig. S14. (a) EPR spectra and (b) Yield of CO and O_2 of 0.6Au/BOB and 0.6Au/BOB-350°C.

Fig. S15. Photocatalytic CO evolution stability experiment of 0.6Au/BOB.

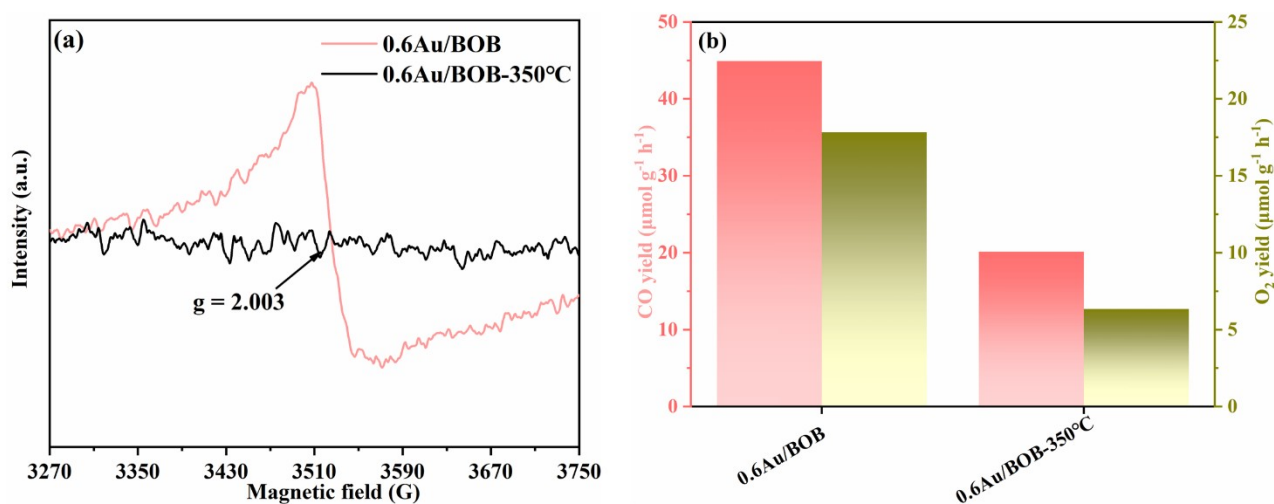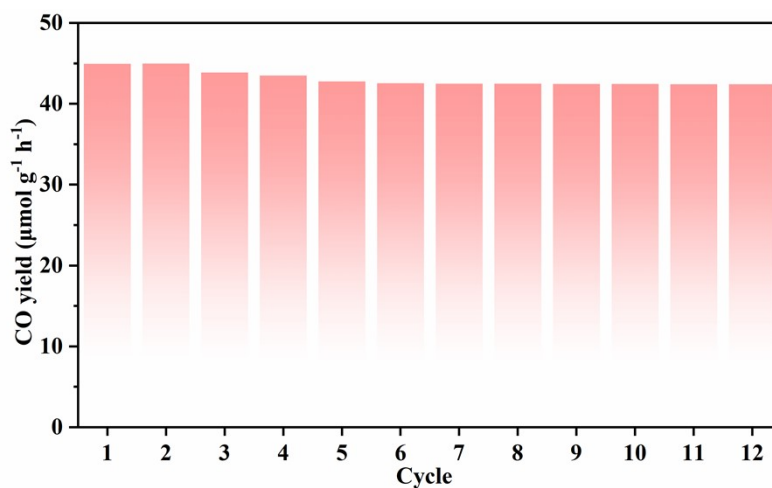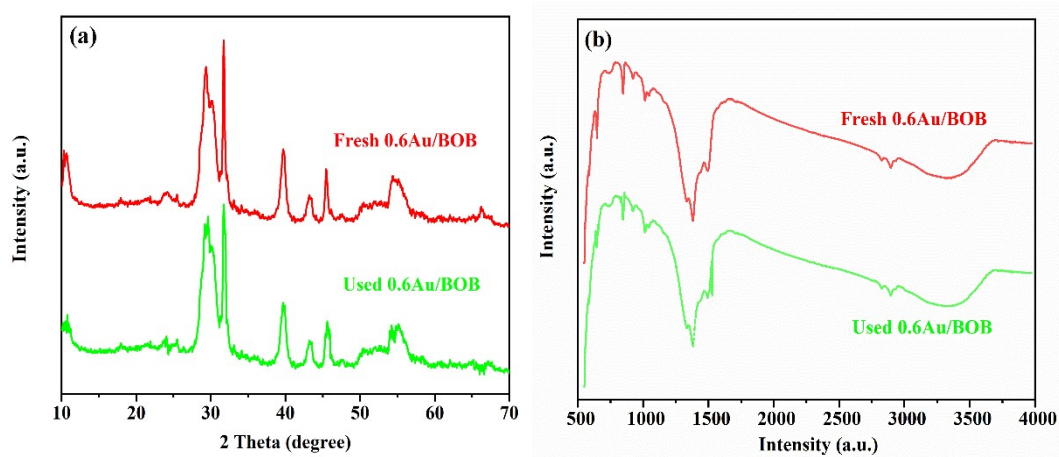**Fig. S16.** (a) XRD patterns and (b) FTIR spectra of the fresh and used 0.6Au/BOB.
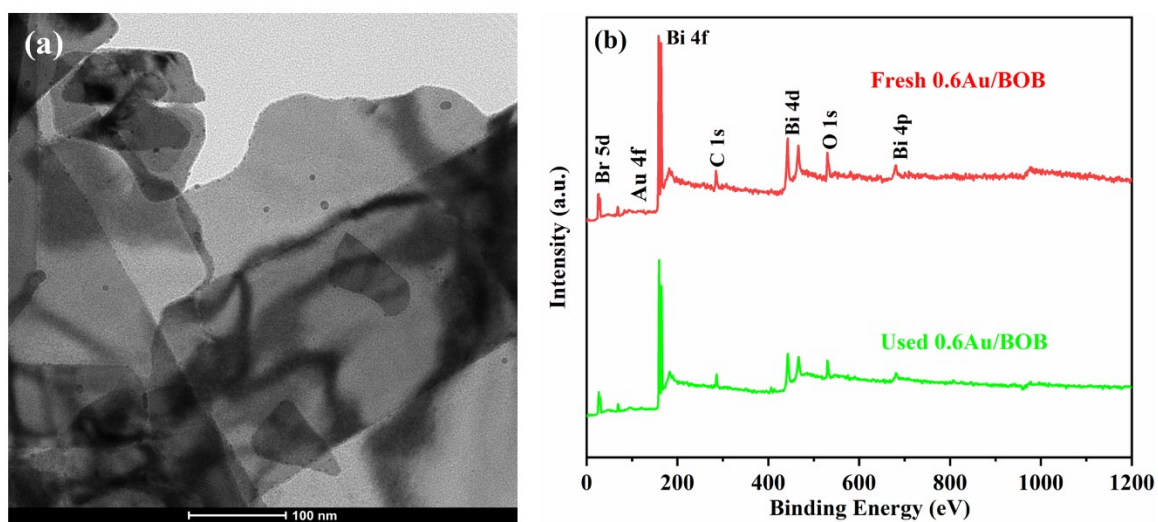
Fig. S17. (a) EPR spectra and (b) Yield of CO and O_2 of 0.6Au/BOB and 0.6Au/BOB-350℃.
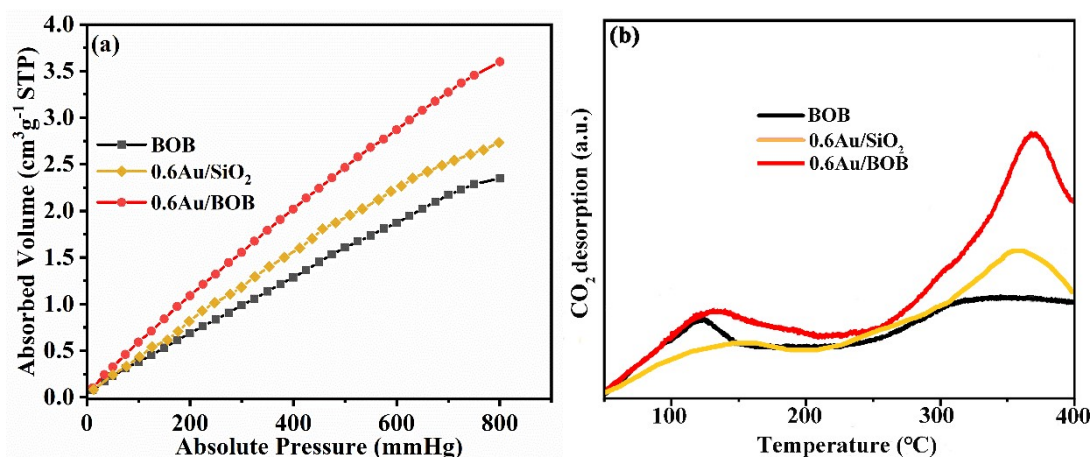
Fig. S18. (a) CO_2 adsorption isotherms; (b) CO_2-TPD of BOB, 0.6Au/SiO$_2$ and 0.6Au/BOB.

The adsorption and activation of CO_2 play an important factor affecting the performance of photocatalytic reduction of CO_2. CO_2 adsorption and CO_2 temperature programmed desorption (CO_2-TPD) were characterized [4]. As shown in **Fig. S18a**, 0.6Au/BOB has higher CO_2 adsorption capacity than 0.6Au/SiO$_2$ and naked BOB, which is beneficial to CO_2 activation. **Fig. S18b** displays that BOB has a new desorption peak near 125 °C, which belongs to the category of weak base peak, showing that BOB has CO_2 adsorption capacity. 0.6Au/SiO$_2$ has two desorption peaks at 160 °C and 360 °C [5], the former belongs to weak base peak and the latter belongs to strong base peak, and the appearance of the latter is related to the loading of noble metal. Therefore, the appearance of strong base desorption peak of 0.6Au/BOB at 380 °C is related to the loading of Au NPs, which means that there are at least two adsorption sites on the surface of 0.6Au/BOB, and the peak intensity of strong base increases, which further proves that Au NPs can really improve the adsorption and activation of CO_2. Therefore, 0.6Au/BOB is more favorable for CO_2 adsorption.

In addition, the active intermediates involved in the conversion of CO_2 to CO were studied by In-situ FTIR. Before the measurement, the impurity species on the surface of the catalyst were removed with argon. At the beginning of the measurement, the wet CO_2 was put into the in-situ cell, and then the active species adsorbed on the catalyst surface was observed in dark and light, respectively. As

shown in **Fig. S19a**, the characteristic vibrational bands of BOB near 1273 and 1671 cm^{-1} are identified as CO_2^- [6]. The vibrational bands near 1299 belong to $m\text{-}CO_3^{2-}$ and the vibrational bands near 1603 cm^{-1} are assigned to $b\text{-}CO_3^{2-}$ [7]. The absorption bands near 1383 and 1626 cm^{-1} correspond to HCO_3^- and H_2O [8], respectively. In addition, the vibrational bands near 1529 and 1637 cm^{-1} belong to *COOH [8]. As shown in **Fig. S19b**, compared with BOB, 0.6Au/BOB composite exhibits the same characteristic vibration band. Moreover, with the extension of light time, the accumulation of active species on 0.6Au/BOB is faster than that BOB, which means that Au NPs promote the generation of active intermediates. Overall, CO_2^-, $m\text{-}CO_3^{2-}$, $b\text{-}CO_3^{2-}$ and *COOH belong to the active intermediates involved in the conversion of CO_2 to CO. In this one, *COOH is a key active species for CO generation[10].

Furthermore, the Gibbs free energies of BOB and 0.6Au/BOB in each stage of photocatalytic CO_2 reduction were also calculated by density functional theory, which is convenient to explore the reduction process of CO_2 at atomic level. Based on the results of in-situ FTIR, four continuous reaction paths are proposed as follows: (1) CO_2 molecules are adsorbed on the surfaces of the catalyst; (2) $*CO_2$ and *H accept the electrons to form the *COOH intermediate; (3) The *COOH intermediate accepts a proton and removes H_2O molecules to form *CO; And (4) *CO will be desorbed to produce CO, and the catalyst will also be restored to the initial state [4]. As shown in **Fig. 19c**, the barriers of BOB at steps (1) (3) and (4) belongs to negative feedback, which proves that these reactions can be carried out spontaneously ($\Delta G<0$). However, step (2) has a reaction barrier as high as 2.60 eV, directly confirming that it belongs to the rate-determining step of BOB. By comparison, 0.6Au/BOB has the same rate-determining step, but its potential barrier is only 0.74 eV, which means that it is easier to accumulate

*COOH intermediates under the same conditions, and then complete the transformation of CO efficiently, which is consistent with the results of in-situ FTIR.
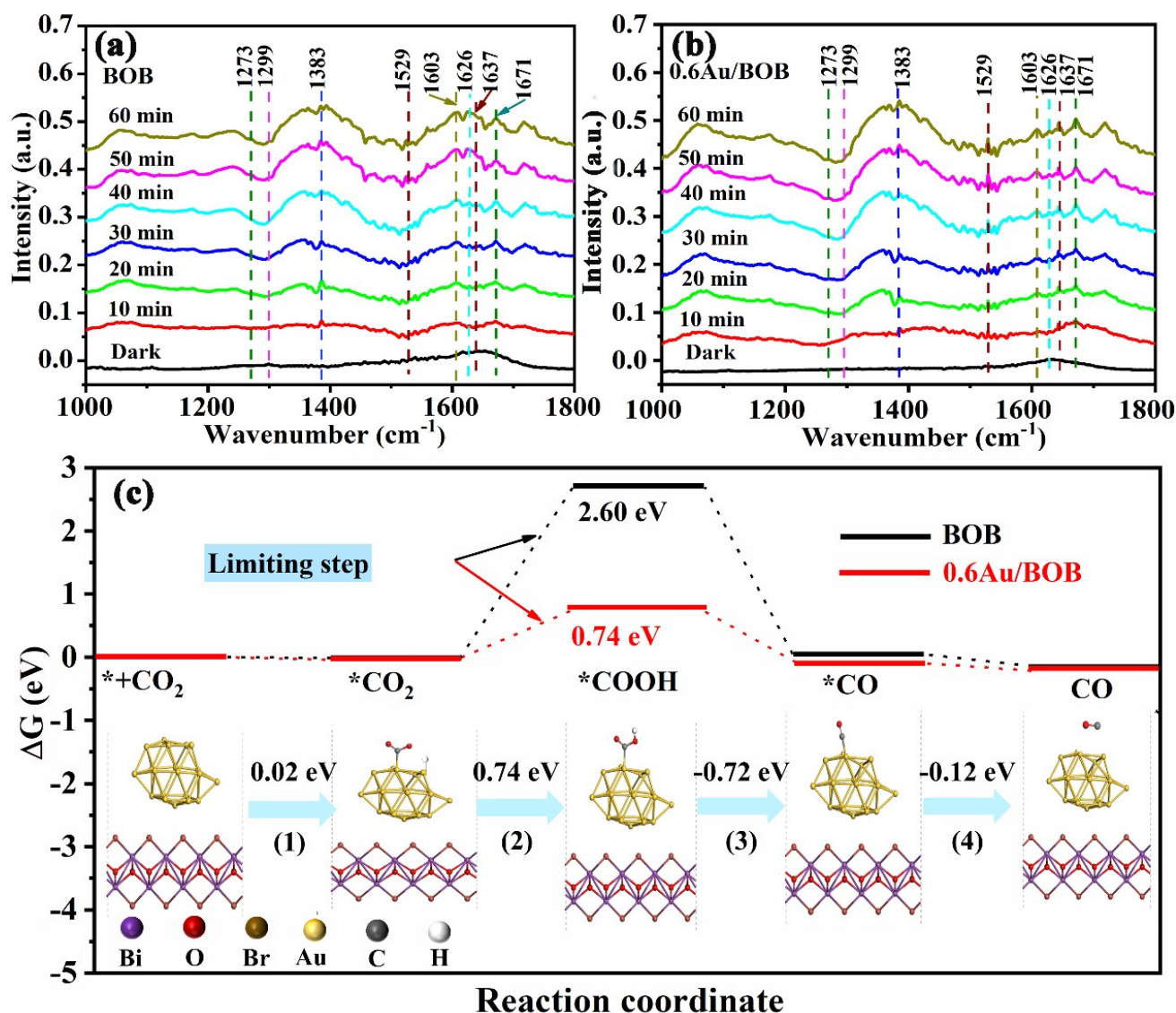
Fig. S19. In-situ FTIR of CO_2 adsorption over (a) BOB and (b) 0.6Au/BOB under visible light irradiation; (c) Calculated free energy diagrams for BOB and 0.6Au/BOB (where "*" represents the adsorption state).

Table S1. Au NPs content in Au/BOB composite was measured by ICP.

content	0.3Au/BOB	0.6Au/BOB	1.2Au/BOB
Theoretical content (wt%)	0.3	0.6	1.2
Experimental content (wt%)	0.27	0.56	1.18

Table S2. Specific surface area, pore diameter and pore volume of BOB, 0.3Au/BOB, 0.6Au/BOB

and 1.2Au/BOB.

Samples	S_{BET} (m^{2}g^{-1})	Pore diameter (nm)	Pore volume (cm^{3}g^{-1})
BOB	3.995	27.477	0.024977
0.3Au/BOB	5.636	28.663	0.43598
0.6Au/BOB	7.874	33.774	0.066485
1.2Au/BOB	9.634	32.117	0.67145

Table S3. Lifetime profile and corresponding carrier dynamics information of the synthesized photocatalysts.

Samples	τ_1 (ns)	τ_1 (ns)	A_1	A_2	Average lifetime τ_{av} (ns)
BOB	0.472158	3.08299	684.702	28.3929	1.02
0.6Au/BOB	0.511661	3.52445	693.048	55.3426	1.58

The average fluorescence lifetimes of BOB and 0.6Au/BOB are calculated by the following formula:

$$\tau_{av} = \frac{A_1 \times \tau_1^2 + A_2 \times \tau_2^2}{A_1 \times \tau_1 + A_2 \times \tau_2} \qquad (9)$$

Where A_1 and A_2 are amplitude constants, τ_1 and τ_2 are fluorescence lifetime components, and τ_{av} represents average fluorescence lifetime.

Action spectra analysis is a plot of apparent quantum yield (AQY) against incident light wavelength, which can be used for reflecting the light absorption and conversion ability of efficient photocatalyst. Therefore, the CO evolution per unit time of 0.6Au/BOB under different monochromatic light (λ=380, 420, 470 and 570 nm) was tested, and the light power of 300 W Xe lamp with different bandpass filter were measured by PL-MW2000 photoradiometer, with the probe area of 1×1 cm^2 to contact light. The irradiation area was controlled as 19.75 cm^2. The test results and the detailed calculation equation of AQY are displaying as follows (**Table S4**), which has also been presented in the Supporting Information of our manuscript.

$$AQE = \frac{N_e}{N_p} \times 100\% = \frac{2 \times M \times N_A \times h \times c}{S \times P \times t \times \lambda} \times 100\%$$

where N_e is the amount of reaction electron, N_p is the incident photon, M is the amount of H_2 molecule, N_A is Avogadro constant, h is the Planck constant, c is the speed of light, S is the irradiation area, P is the intensity of the irradiation, t is the photoreaction time, and λ is the wavelength of the monochromatic light.

Table S4. Calculated apparent quantum efficiency (AQE) of 0.6Au/BOB under light irradiation with different wavelengths.

λ (nm)	CO production in 1hour (µmol)	Light power (W)	AQE
380	8.53	0.038	0.64%
420	6.32	0.041	0.41%
470	2.12	0.056	0.081%
570	1.02	0.022	0.12%

Table S5. Comparison of the photocatalytic CO_2 reduction activity and CO selectivity of various BiOBr-based photocatalysts

Catalysts	CO (µmolg^{-1}h^{-1})	Selectivity (%)	Model	Light (nm)	Reference
BiOBr	1.55	100	gas-solid	Xe, $\geq$ 300	[9]
BiOBr/CdS	4.53	100	pure water	Xe, $\geq$420	[10]
Gd^{3+}/BiOBr	8	16	pure water	Xe, $\geq$420	[11]
2D Bi$_4$O$_5$Br$_2$	2.75	57	gas-solid	Xe, $\geq$400	[12]
3D Bi$_4$O$_5$Br$_2$	3.11	86	gas-solid	Xe, $\geq$300	[13]
C$_3$N$_4$/BiOBr/Au	2.63	83	gas-solid	Xe, $\geq$380	[14]
BiPO$_4$/BiOBr	3.11	83	gas-solid	Xe, $\geq$400	[15]

Material	Rate	Selectivity	System	Light Source	Ref.
$Bi_4O_5Br_2$/AgBr	6.6	78	gas-solid	Xe, ≥300	[16]
UiO-66/$Bi_4O_5Br_2$	8.35	100	pure water	Xe, ≥300	[17]
Bi_2MoO_6 nanosheets	3.6	100	pure water	Xe, ≥300	[18]
g-C_3N_4 QDs/Au NPs/CeO_2/Fe_3O_4	9.3	74	pure water	Xe, ≥300	[19]
Au NPs/g-C_3N_4	0.77	100	pure water	Xe, ≥420	[20]
45%CdS/TiO_2	1.97	83.3	pure water	Hg, ≥350	[21]
TiO_2/NG HS	8.7	48.1	gas-solid	Xe, ≥ 300	[22]
TiO_{2-x}/$W_{18}O_{49}$	3.97	100	gas-solid	Xe, ≥350	[23]
CdS-P25/ZIF-67	29.8	48.8	gas-solid	Xe, ≥320	[24]
CTU/CdS-P25	23.8	100	pure water	Xe, ≥300	[25]
3DOM-CNPTC	14.7	18.3	gas-solid	Xe, ≥420	[26]
TiO_2@$ZnIn_2S_4$ CSHS	9.28	51.1	gas-solid	Xe, ≥ 300	[27]
BOB	9.3	100	pure water	Xe, ≥420	This work
0.6Au/BOB	44.92	100	pure water	Xe, ≥420	This work

Reference

1   S. Sun, X. Wu, Z. Huang, H. Shen, H. Zhao and G. Jing, *Chem. Eng. J.*, 2022, **435**, 135035.

2   Y. Qin, H. Li, J. Lu, F. Meng, C. Ma and Y. Yan, *Chem. Eng. J.*, 2020, **384**, 123275.

3   T. Han, X. Cao, K. Sun, Q. Peng, C. Ye, A. Huang, W. C. Cheong, Z. Chen, R. Lin, D. Zhao, X. Tan, Z. Zhuang, C. Chen, D. Wang and Y. Li, *Nat. Commun.*, 2021, **12**, 1–11.

4   K. Wang, M. Cao, J. Lu, Y. Lu, C. H. Lau, Y. Zheng and X. Fan, *Appl. Catal. B Environ.*, 2021, **296**, 120341.

5   H. X. Zhang, S. W. Chen, X. Y. Cui, D. H. Pan, Z. F. Qin and J. G. Wang, *Wuli Huaxue Xuebao/ Acta Phys. - Chim. Sin.*, 2014, **30**, 351–358.

6   L. Liu, F. Gao, H. Zhao and Y. Li, *Appl. Catal. B Environ.*, 2013, **134–135**, 349–358.

7   C. Zhang, Y. Wang, X. Zhang, R. Wang, L. Kou, J. Wang, R. Li and C. Fan, *Chem. Eng. J.*, 2021, **417**, 128218.

8   X. Li, Y. Wei, C. Ma, H. Jiang, M. Gao, S. Zhang, W. Liu, P. Huo, H. Wang and L. Wang, *ACS Appl. Mater. Interfaces*, 2021, **13**, 11755–11764.

9   M. Gao, J. Yang, T. Sun, Z. Zhang, D. Zhang, H. Huang, H. Lin, Y. Fang and X. Wang, *Appl. Catal. B Environ.*, 2019, **243**, 734–740.

10   Q. Yang, W. Qin, Y. Xie, K. Zong, Y. Guo, Z. Song and G. Luo, *Sep. Purif. Technol.*, 2022, **298**, 121603.

11   W. Jiao, Y. Xie, F. He, K. Wang, Y. Ling, Y. Hu, J. Wang, H. Ye, J. Wu and Y. Hou, *Chem. Eng. J.*, 2021, **418**, 129286.

12   L. Ye, X. Jin, C. Liu, C. Ding, H. Xie, K. H. Chu and P. K. Wong, *Appl. Catal. B Environ.*, 2016, **187**, 281–290.

13   X. Jin, C. Lv, X. Zhou, H. Xie, S. Sun, Y. Liu, Q. Meng and G. Chen, *Nano Energy*, 2019, **64**, 103955.

14   Y. Bai, T. Chen, P. Wang, L. Wang, L. Ye, X. Shi and W. Bai, *Sol. Energy Mater. Sol. Cells*, 2016, **157**, 406–414.

15   J. Liu, M. Wu, H. Ye, Y. Xie, Y. Ma and L. Liu, *Chem. Eng. J.*, 2023, **455**, 140722.

16   X. Jin, J. Cao, H. Wang, C. Lv, H. Xie, F. Su, X. Li, R. Sun, S. Shi, M. Dang and L. Ye, *Appl. Surf. Sci.*, 2022, **598**, 153758.

17   D. Li, B. Zhu, Z. Sun, Q. Liu, L. Wang and H. Tang, *Front. Chem.*, 2021, **9**, 1–10.

18   J. Di, X. Zhao, C. Lian, M. Ji, J. Xia, J. Xiong, W. Zhou, X. Cao, Y. She, H. Liu, K. P. Loh, S. J. Pennycook, H. Li and Z. Liu, *Nano Energy*, 2019, **61**, 54–59.

19   Y. Wei, X. Li, Y. Zhang, Y. Yan, P. Huo and H. Wang, *Renew. Energy*, 2021, **179**, 756–765.

20   D. Wang, Y. Li, B. Yu, H. Li, W. Jiang, X. Deng, Y. Wen, C. Liu and G. Che, *Adv. Powder Technol.*, 2021, **32**, 1653–1662.

21   A. Ahmad Beigi, S. Fatemi and Z. Salehi, *J. CO$_2$ Util.*, 2014, **7**, 23–29.

22   L. Wang, B. Zhu, B. Cheng, J. Zhang, L. Zhang and J. Yu, *Chinese J. Catal.*, 2021, **42**, 1648–1658.

23   J. Z. Y. Tan, S. Gavrielides, M. Belekoukia, W. A. Thompson, L. Negahdar, F. Xia, M. M. Maroto-Valer and A. M. Beale, *Chem. Commun.*, 2020, **56**, 12150–12153.

24   L. Wang, Z. Zhang, Q. Han, Y. Liu, J. Zhong, J. Chen, J. Huang, H. She and Q. Wang, *Appl. Surf. Sci.*, 2022, **584**, 152645.

25   R. Lian, L. Wang, Y. Gao, J. Zhang, Q. Mei and Q. Wang, *J. Alloys Compd.*, 2022, **924**, 166590.

26   C. Wang, X. Liu, W. He, Y. Zhao, Y. Wei, J. Xiong, J. Liu, J. Li, W. Song, X. Zhang and Z. Zhao, *J. Catal.*, 2020, **389**, 440–449.

27   L. Wang, B. Cheng, L. Zhang and J. Yu, *Small*, 2021, **17**, 1–9.